Multiple molecular architectures of the eye lens chaperone B-crystallin elucidated by a triple hybrid approach

Multiple molecular architectures of the eye lens chaperone αB-crystallin elucidated by a triple hybrid approach

Nathalie Braun[a], Martin Zacharias[b], Jirka Peschek[a], Andreas Kastenmüller[a], Juan Zou[c], Marianne Hanzlik[a], Martin Haslbeck[a], Juri Rappsilber[c], Johannes Buchner[a], and Sevil Weinkauf[a,1]

[a]Center for Integrated Protein Science Munich, Chemistry Department, Technische Universität München, Lichtenbergstrasse 4, 85747 Garching, Germany; [b]Physics Department, Technische Universität München, James-Franck-Strasse 1, 85747 Garching, Germany; and [c]Wellcome Trust Centre for Cell Biology, School of Biological Sciences, University of Edinburgh, Edinburgh EH9 3JR, Scotland, United Kingdom

Edited by* Wolfgang P. Baumeister, Max Planck Institute of Biochemistry, Martinsried, Germany, and approved October 21, 2011 (received for review July 8, 2011)

The molecular chaperone αB-crystallin, the major player in maintaining the transparency of the eye lens, prevents stress-damaged and aging lens proteins from aggregation. In nonlenticular cells, it is involved in various neurological diseases, diabetes, and cancer. Given its structural plasticity and dynamics, structure analysis of αB-crystallin presented hitherto a formidable challenge. Here we present a pseudoatomic model of a 24-meric αB-crystallin assembly obtained by a triple hybrid approach combining data from cryoelectron microscopy, NMR spectroscopy, and structural modeling. The model, confirmed by cross-linking and mass spectrometry, shows that the subunits interact within the oligomer in different, defined conformations. We further present the molecular architectures of additional well-defined αB-crystallin assemblies with larger or smaller numbers of subunits, provide the mechanism how "heterogeneity" is achieved by a small set of defined structural variations, and analyze the factors modulating the oligomer equilibrium of αB-crystallin and thus its chaperone activity.

The most prominent member of the small heat-shock protein (sHsp) family, α-crystallin, is expressed at high concentrations in the vertebrate eye lens (1) where it plays a major role in maintaining lens transparency (2). Moreover, it protects lens epithelial cells from environmental stress by preventing aggregation of stress-damaged proteins (3). In the low protein turnover milieu of the eye lens, proteins gradually deteriorate throughout the lifespan due to posttranslational modifications and become increasingly prone to aggregation leading to opacity. Thus, the chaperone action of α-crystallin is vital for maintaining the eye lens transparency. Lenticular α-crystallin is composed of two homologous polypeptides, αA- and αB-crystallin, which comprise 173 and 175 amino acid residues, respectively (1, 4). Both proteins possess a three-domain organization consisting of the α-crystallin domain (ACD), a consensus sequence of approximately 90 amino acids common to all sHsps, flanked by a diverse N-terminal region and a moderately conserved C-terminal extension (5, 6).

Of the two constituents of α-crystallin, αB-crystallin is the more widespread chaperone with versatile functions: Besides the eye lens, it is abundantly expressed in other tissues (7) and upregulated by various stresses (8). There is growing evidence for its implications in several neuropathological diseases (9) including Parkinson disease, Alzheimer's disease, and multiple sclerosis (10, 11) as well as in cancer (12). In vitro, αB-crystallin prevents the stress-induced aggregation of partially folded polypeptides (3, 13).

The αB-crystallin assembles into homooligomers with a variable number of subunits, primarily 24–32 (14–16), and the subunits exchange between homooligomers (17). These properties have hampered high-resolution structural studies on the functionally assembled, full-length protein. An earlier cryoelectron microscopy (cryo-EM) study (18) presented at low resolution (36 Å) a 32-meric assembly as an asymmetric structure with a large central cavity and suggested the presence of multiple assemblies of highly variable quaternary structures. In our previous work on human recombinant αB-crystallin utilizing negative stain-EM, we characterized the 3D structure of the dominant 24-mer (13). The 3D model at 20-Å resolution disclosed a spherical, symmetric protein shell with fenestrations, an architecture similar to other sHsps (19, 20). Crystallographic and NMR studies on truncated forms of human αB-crystallin (21–23) as well as on the full-length protein (23) revealed the structures of ACD dimers, their pH-dependent architectures, and gave hints on intersubunit interactions. A recent study (24) suggested an atomic-level model of a full-length αB-crystallin 24-mer based on data from NMR, small angle X-ray scattering, and on our negative stain-EM model (13). Nevertheless, due to the insufficient accuracy of the protein envelope obtained from negative stain-EM, which per se reflects only molecular surfaces accessible to stain and lack internal structural information, the full assembly pattern remained speculative.

Here we present a pseudoatomic model of the full-length αB-crystallin 24-mer obtained by cryo-EM together with structural modeling and validated by cross-linking/mass spectrometry studies. Based on the molecular architectures of the 24-mer and additional well-defined oligomers, we provide the assembly principles of αB-crystallin and the mechanism how heterogeneity is achieved only by a few structural variations. We further analyze the factors modulating the oligomer equilibrium of αB-crystallin and thus its chaperone activity.

Results and Discussion

Structure of the αB-Crystallin 24-mer. On cryo-EM micrographs, αB-crystallin oligomers showed size and structural variability (Fig. S1). Upon an initial single particle analysis, approximately 30% of the whole dataset were assigned to 24-meric αB-crystallin and were used to calculate several 3D reconstructions (Fig. S2) (for details see *SI Materials and Methods*) which finally yielded a 3D model for the 24-mer at 9.4-Å resolution (Fig. 1).

According to the reconstructed EM volume, which is reminiscent of the one obtained from negatively stained single particles

Author contributions: N.B., J.B., and S.W. designed research; N.B., M.Z., J.P., A.K., J.Z., M. Hanzlik, M. Haslbeck, J.R., and S.W. performed research; N.B., M.Z., J.P., J.Z., J.R., and S.W. analyzed data; and N.B., M.Z., J.R., J.B., and S.W. wrote the paper.

The authors declare no conflict of interest.

*This Direct Submission article had a prearranged editor.

Freely available online through the PNAS open access option.

Data deposition: The cryo-EM density map of αB-crystallin 24-mer has been deposited in the Electron Microscopy Data Bank, http://www.ebi.ac.uk/pdbe/emdb/ (accession no. EMD-1894). The pseudoatomic model of the 24-mer has been deposited in the Protein Data Bank in Europe, http://www.pdbe.org/emdb (PDB ID code 2YGD).

[1]To whom correspondence should be addressed. E-mail: sevil.weinkauf@tum.de.

This article contains supporting information online at www.pnas.org/lookup/suppl/doi:10.1073/pnas.1111014108/-/DCSupplemental.

BIOCHEMISTRY

(13), the αB-crystallin 24-mer is a hollow, spherical complex of approximately 13.5-nm diameter (Fig. 1*A*). The protein envelope, in which the subunits are arranged according to tetrahedral symmetry, varies in thickness from 1.5 to 4.0 nm. The central cavity is accessible through narrow and elongate openings at positions of the twofold symmetry axes (Fig. 1*A*, *Left*) and almost round ones at one of the two areas where a threefold symmetry axis intercepts the protein shell ("open" threefold area, 3_o) (Fig. 1*A*, *Center*). The area around 3_o has a pronounced relief where three "domes" run together. Most notable, however, is the distinct mass accumulation at the position of the opposite intercept of the threefold axis ("closed" threefold area, 3_c) (Fig. 1*A*, *Right*), a key structure element which was not visible in the reconstruction from negatively stained particles (13). Within this area, several relatively straight rods of densities corresponding to α-helical segments of the structure are clearly distinguishable (Fig. 1*D*).

The improvement in resolution allowed us to generate a pseudoatomic model of the 24-mer by a triple hybrid approach in which the structure of the ACD from NMR (23) and our predicted structures of C and N termini in their entire lengths (Fig. S3) were integrated into the cryo-EM density map (Fig. 1*C*). During docking, only the constraints given by the EM envelope and interactions seen by NMR (23) were taken into account. The cross-correlation coefficient of the fit at the attained resolution was 0.83, indicating an excellent agreement between the density map and the fitted structure.

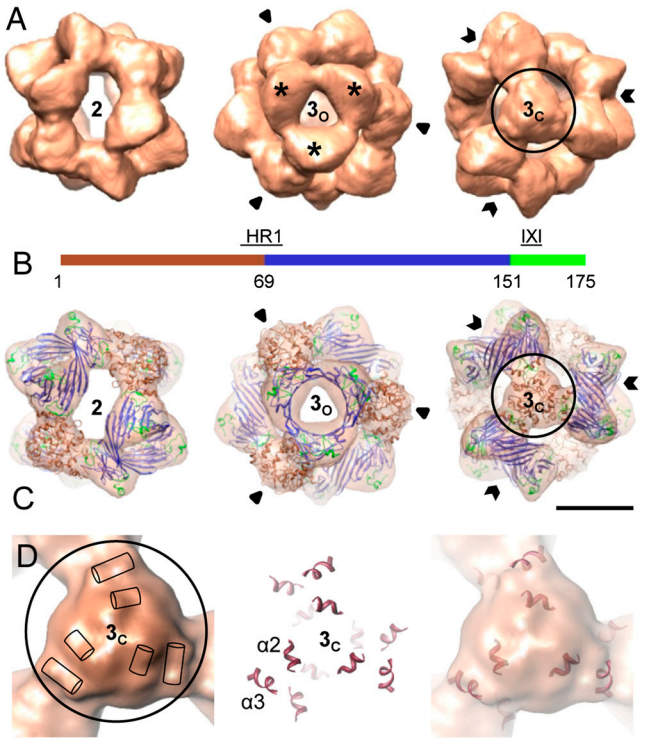

Fig. 1. Three-dimensional model of the αB-crystallin 24-mer. (*A*) Surface representations of the cryo-EM density map viewed along a two- (*Left*) and a threefold symmetry axis intercepting the area harboring a "window" (3_o, open arrows) (*Center*), and mass accumulation (3_c, closed arrows) (*Right*). Mass-rich domes surrounding 3_o are highlighted by stars. The isosurface threshold was set to enclose a molecular mass of 485 kDa. (*B*) Domain organization of human αB-crystallin: N-terminal segment (residues 1–68) (brown), ACD (residues 69–150) (blue), C-terminal region (residues 151–175) (lime green). The heterogeneous region 1 (HR1) and the IXI motif are indicated. (*C*) Views of the oligomer with the docked hybrid model of αB-crystallin 24-mer (ribbon representation) superimposed. Ribbon color coding is the same as in *B*. (Scale bar, 5 nm.) (*D*) Close-up view of the density map at the area 3_c (*Left*). The positions of the rod-like densities are schematically indicated by cylinders. Surface near helices in the pseudoatomic model (*Center*) superposed on the cryo-EM density map (*Right*).

In order to assess the validity of our model and to determine the actual intra- and intermolecular spatial proximities of residues, especially in the N- and C-terminal domains of αB-crystallin, we applied cross-linking in conjunction with mass spectrometry (25, 26). Using bis[sulfosuccinimidyl]suberate (BS3) as a cross-linker that mainly targets primary amino groups of lysine side chains and the protein N termini but also hydroxyl groups of serine and threonine side chains (Fig. S4*A*), we were able to identify several intra- and intermolecular cross-links (Fig. S4*C*). The distances extracted from the model between cross-linked residue pairs all turned out to be below the upper distance limit of 27.4 Å dictated by the cross-linker and indicated the overall validity of the proposed pseudoatomic model for αB-crystallin 24-mer.

Our model reveals that the recurring unit of the 24-mer is a hexameric substructure around the area 3_o in which αB-crystallin monomers are arranged in an alternating pattern of two interrelated conformations (Fig. 2*A*) (see also *SI Materials and Methods*). In one conformer, the ACD and N-terminal region enclose an angle of 55° giving the monomer a bent shape ("bent monomer," M_b) and setting its N and C termini at opposite ends (Fig. 2*B* and Fig. S3). In the other conformer ("extended monomer," M_e), they are arranged almost linearly, allowing intramolecular interactions between N and C termini (Fig. 2*B* and Fig. S3) as also evidenced in the observed intramolecular cross-links (Fig. 2*C* and Fig. S4). The orientation of the N terminus in M_b is mainly determined by a turn comprising residues E71–R74, which reverses the direction of the polypeptide chain by 145° as compared to that in M_e (Fig. 2*D*). The C terminus of M_b extends at its extremity (R163–K175) into the dome (Fig. 2*B*) and is fully solvent-exposed. This observation is in agreement with the results from fluorescence quenching experiments where the lucifer yellow-labeled cysteine variant A172C showed the highest accessibility for the quencher (Fig. S5*A*). The ample electron density in this area suggests considerable flexibility of the very C-terminal residues in agreement with previous NMR

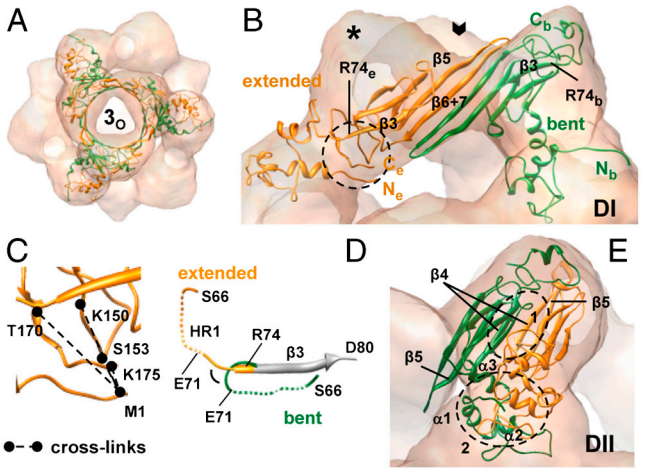

Fig. 2. The αB-crystallin adopts in the 24-mer two different conformations. (*A*) The αB-crystallin hexamer (ribbon diagram) viewed along a threefold symmetry axis. Conformationally different monomers extended (M_e) and bent (M_b) are shown in orange and green, respectively. (*B*) Spatial arrangement of M_e and M_b in type I dimer (DI). Open arrow indicates the position of a threefold axis (3_o). The residue R74 is labeled on both conformers. The area highlighted by a circle encloses the N and C termini of M_e. (*C*) Enlarged view of the encircled area in *B* with the intramolecular cross-links between M1 and C-terminal residues of M_e. (*D*) Close-up view of the region S66-D80. The β3 strands (residues 74–79) of M_e and M_b are aligned and partly shown in gray. Dashed lines: HR1 regions (E67–L70 corresponding to the β2 strand in other sHsps) of M_e and M_b. Note the different environments for HR1 in both conformers. (*E*) Spatial arrangement of M_e and M_b in type II dimer (DII). Close-up views of DII interface patches 1 and 2 highlighted by circles are shown in Fig. 3.

observations (27). The very C terminus of M_e points toward the twofold symmetry axis and is involved in intramolecular contacts to the N-terminal region (Fig. 2 *B* and *C*).

The model also reveals two types of dimers in the oligomer, which differ in their intersubunit contacts relevant for the stabilization of the hexameric unit. In the type I dimer (DI) (Fig. 2*B*), M_e and M_b interact through their β6 + 7 strands within ACDs as previously described (23). The dimer interface is localized in the cleft between the two domes surrounding 3_o and covers an area of approximately 860 Å^2 (Fig. 2*B*). The concave surface of the curved dimer interface with a network of ionic interactions faces the opening at the area 3_o (Fig. 3*A*). In the type II dimer (DII) (Fig. 2*E*), the interface consists of several patches collectively forming an interface surface area of approximately 2,700 Å^2 where different domains contribute to subunit interactions. Within the ACD, β4 strands of M_e and M_b align at their edges in an antiparallel fashion and form also a curved surface containing charged amino acid residues facing the opening at 3_o (Fig. 3*B*). Both conformers further interact through the binding of their IXI motifs (I159-P160-I161) to the hydrophobic groove formed by the β4- and β8-strands of the other monomer

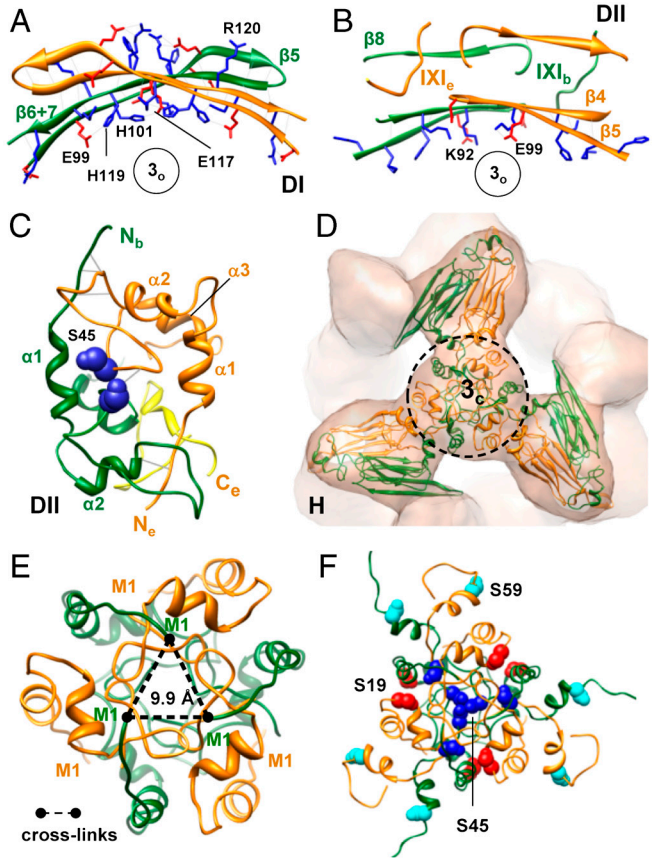

Fig. 3. Subunit interfaces in the αB-crystallin 24-mer. (*A*) DI interface viewed along a threefold axis (for the spatial arrangement and localization of the type I dimer see Fig. 2*B*). Positively and negatively charged residues of the β5 and β6 + 7 strands are shown in blue and red, respectively. (*B*) DII interface patch formed by the ACDs of both conformers (area 1 in Fig. 2*E*). Charged residues of the β4 and β5 strands and segments of both protomers containing the IXI motifs are shown. (*C*) DII interface patch encompassing the N- and C-terminal domains of both conformers (area 2 in Fig. 2*E*). S45 residues of both conformers are shown as spheres in dark blue. The C terminus of the extended monomer is colored yellow. (*D*) Hexamer assembly site at the area 3_c. For close-up views of the encircled area see *E* and *F*. (*E*) Intermolecular cross-links between the N termini of bent monomers at the hexamer assembly site. (*F*) Location of the N-terminal serine residues within the hexamer assembly area. The serine residues 19, 45, and 59 are shown as spheres and are colored in red, dark blue, and cyan, respectively.

(23, 28) (Fig. 3*B*). In addition, hydrophobic interactions between N-terminal domains of both conformers as well as electrostatic interactions between the C terminus of M_e and the N-terminal segment R56–D62 of M_b contribute to dimer formation (Fig. 3*C*). The extensive involvement of the C-terminal extension in intersubunit interactions is in line with studies on truncation mutants of αA- and αB-crystallin which show that the cleavage of more than 10 C-terminal residues results in a decrease in the oligomer size (29).

According to our model, the association of the hexameric substructures in the 24-mer is mediated via interactions of the N termini of three type II dimers at the area 3_c (Fig. 3*D*). The N termini do not point toward the interior of the oligomer, as proposed recently (24), because this would give rise to an additional density within the cavity, which is definitely absent in the cryo-EM map. The close coincidence of the predicted N-terminal α-helices in our energy-minimized model with the rods of densities observed in the cryo-EM map (Fig. 1*D*), as well as the intermolecular linkage of N-terminal methionins (M1) evidencing their close proximity (Fig. 3*E* and Fig. S4) further support the structure prediction for the N-terminal regions as well as their locations, especially as no constraints were applied in this respect during docking. Nevertheless, as the pseudoatomic model is based on an averaged 3D density, a certain degree of N-terminal flexibility cannot be ruled out.

The predicted interactions between N termini at the hexameric interface are mediated by side chains of loop regions and possibly involve solvent molecules that fill cavities and voids at the interface. The core of the interface is dominated by hydrophobic residues, whereas the rim region contains an excess of negatively charged residues. The three major phosphorylation sites of αB-crystallin in vivo (30)—S19, S45, and S59—are all located within the area of hexamer contacts and have different accessibilities (Fig. 3*F*). Whereas S59 from both conformers and S19 of M_e are distributed peripherally on the surface of the 24-mer, S19 from M_b faces the interior (Fig. 3*F*). Most intriguingly, however, S45 residues from M_e and M_b form a dimeric interface patch (Fig. 3*C*) and three such patches arrange in a cluster buried inside the structure (Fig. 3*F*). The exposure of S45 residues would thus require at least the disruption of this dimeric patch and/or disruption of N-terminal interactions, which promote the association of hexamers into the higher-order oligomer. The replacement of S19 and S59 residues by negatively charged amino acids in phosphorylation-mimicking mutants is not very likely to perturb the integrity of the oligomer because they are in close proximity of positively charged residues. In contrast, substitution of S45 by negatively charged residues could destabilize the dimeric interface patch, and hence compromise interactions in the oligomer.

The αB-crystallin 24-mer does not possess large hydrophobic patches on its surface, which could act as binding sites for substrate proteins. There are small hydrophobic patches on the interior wall, however, these are not readily accessible in the oligomer. Notably, both αB-crystallin conformers harbor hydrophobic pockets or patches buried at their DII interfaces (Fig. 4). One such pocket within M_e encompasses parts of the segments 73–92 and 131–141. Both segments are implicated in substrate binding (31) and contribute to the hydrophobic groove that hosts the IXI motif of the neighboring monomer (23, 28) (Fig. 4*A*). One further hydrophobic pocket is formed by I10 and several residues within the N-terminal segment 44–55, which were suggested to be involved in binding of completely unfolded proteins (32). A third pocket is formed by the N-terminal residues 3–5 together with hydrophobic residues of the C-terminal segment encompassing residues 152–171 (Fig. 4*A*), which were shown to be protected from proteolysis in the presence of a substrate protein (33). In a similar manner, M_b hosts at the DII interface the hydrophobic β4/β8 groove and the conserved N-terminal phenylalanine-rich region, which was suggested to be essential for chaperone-like

BIOCHEMISTRY

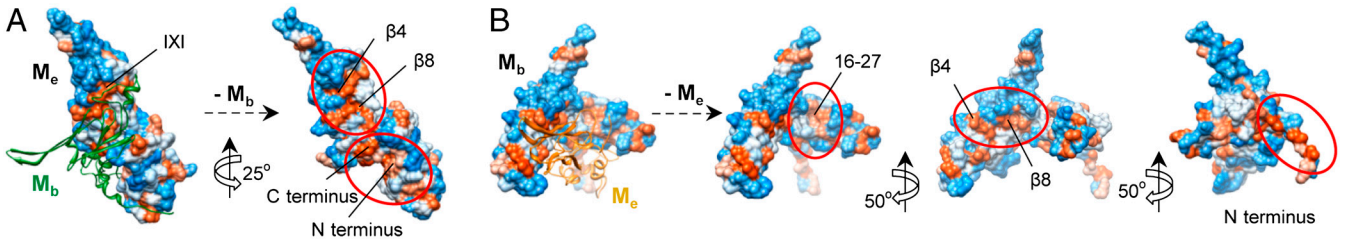

Fig. 4. Hydrophobic patches of αB-crystallin buried at subunit interfaces. (*A*) Hydrophobic patches of an extended monomer (M_e) (hydrophobicity surface) buried by the overlying bent monomer (M_b) (ribbon diagram, green) at the DII interface of the 24-mer. (*B*) Hydrophobic patches of a bent monomer (M_b) (hydrophobicity surface) exposed upon removal of the overlying extended monomer (M_e) (ribbon diagram, orange). Color coding: hydrophilic, blue; neutral, white; hydrophobic, orange.

activity (34) (Fig. 4*B*). A third hydrophobic stretch contains hydrophobic residues at the very N terminus that were identified as a potential target protein binding site protected from proteolysis by the bound substrate (33) (Fig. 4*B*). All described patches become exposed only upon removal of subunits from the 24-mer.

αB-Crystallin Heterogeneity. In the course of 3D reconstruction, we identified asymmetric complexes with varying levels of mass at and close to the 3_c areas (Fig. S6*A*) which constitute the hexamer assembly sites accommodating the N termini of three type II dimers. Random 3D reconstructions with imposed C1 symmetry of such images revealed species with substantial variances in the connectivities between the hexamers ranging up to their complete loss (Fig. S6*D*). These species presumably represent individual conformations adopted by the 24-mer during a process, in which type II dimers disconnect concomitant with the detachment of hexamers. The results further suggest that αB-crystallin hexamers exist in solution as intermediate assemblies, which is in accord with the observation that an αB-crystallin truncation mutant consisting of residues 68–162 forms also hexameric species (22). Sedimentation velocity analytical ultracentrifugation (SV-AUC) experiments show that, in the presence of destabilizing concentrations of guanidine chloride (GdnCl), smaller oligomeric assemblies (e.g., dimers, hexamers, and 12-mers) exist (Fig. S5*B*). These species, presumably present at low abundance in the dynamic oligomer equilibrium under native conditions, seem to become more populated upon the addition of the denaturant.

The presence of hexameric species in solution along with images having dimensions incompatible with the 24-mer prompted us to analyze the cryo-EM data for other oligomers composed of multiples of hexamers. We therefore constructed hypothetical models for 12-, 18-, 36-, and 48-mers with hexameric units as building blocks ($n \times$ 6-mers) (Fig. S6*E*) and used them as initial references to roughly separate the entire data into three subsets. The data subsets covered particles with dimensions (*i*) smaller or (*ii*) larger than and (*iii*) comparable to the dimensions of the 24-mer (Fig. S7). Four-dimensional projection matching cycles within the first two subsets clearly resolved 12-mers in two conformations, as well as 36- and 48-mers (Fig. 5). In the case of 18-mer, however, the reconstructed volume showed an additional density connecting two 3_c areas in the 24-mer (Fig. S6*F*). This density matched perfectly with the density of a dimer consisting of two extended monomers (Fig. S6*G*). Thus, we concluded that the 3D reconstruction corresponded in fact to a 20-mer built of three hexamers and one additional dimeric building block (18-mer + 1 × 2-mer). Based on this observation, we constructed further models of multiples of hexamers complemented with a varying number of dimers each bridging two 3_c areas ($n \times$ 6-mers + $n \times$ 2-mers). This association was also suggested based on interactions seen in NMR spectra (24), which are fulfilled in our models as well. Because a variance analysis of the reconstructions gave indications for missing masses, we also built 24-mer models lacking different types of dimers (DI, DII) or monomers (bent, extended) as well as a 24-mer model imitating hexamer detachment/attachment. Four-dimensional projection matching iterations using all these models as initial references allowed us to unambiguously assign 80% of the particles of the entire cryo-EM data to distinct oligomer populations and to calculate their respective 3D reconstructions (Fig. 5).

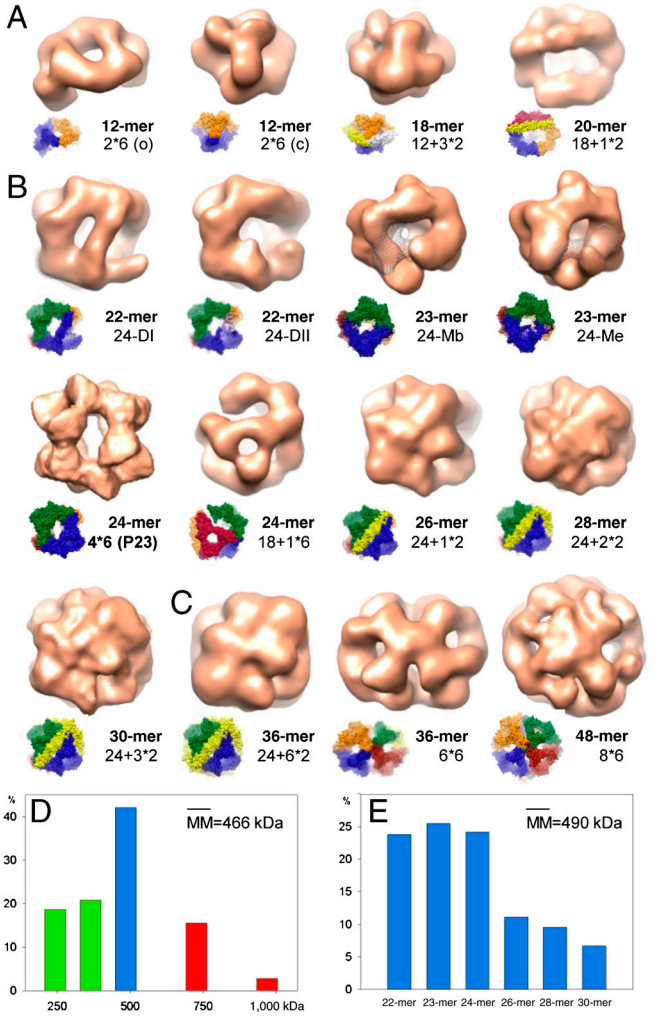

Fig. 5. Three-dimensional reconstructions of αB-crystallin oligomers and their distribution. Oligomers found in the "small" dataset (*A*), in the "24-mer" dataset (*B*), and in the "large" dataset (*C*). (*Insets*) Oligomer models showing the boundaries of hexameric and dimeric building blocks. The missing volume of the monomer in the 23-mers in *B* is highlighted in mesh representation. (*D*) Distribution of the oligomer masses derived from particle size and form distributions obtained upon 4D projection matching cycles applied to datasets small, 24-mer, and large. Particles with molecular masses (MM) corresponding to 12-, 18-, and 20-mers are included in green bars, to the 24-mer in the blue bar, to 36- and 48-mers in red bars. (*E*) Distribution of oligomers within the supposed 24-mer population (blue bar in *D*) determined by 4D projection matching cycles using all 22- to 30-mer pseudoatomic models.

According to our analysis, most of the αB-crystallin oligomers share the remarkably conserved modular architecture of the 24-mer and are built of almost spherical protein shells that enclose a central cavity. Although some of the oligomers show little structural variations presumably representing "robust," less-flexible assembly forms under the given conditions (e.g., 12-mers), others are less populated and less well-structured (e.g., 48-mer), as also indicated by the resolutions of the 3D reconstructions (Table S1).

Within the detection limits of cryo-EM and under our experimental conditions, the dominant species contain even numbers of subunits, consistent with previous results from mass spectrometry (14, 16). The distribution of the oligomer masses derived from the analysis of the initial three data subsets suggests at first sight that oligomers with 24 subunits are clearly favored, followed by such with 18 and 12 subunits (Fig. 5*D*). The mean molecular mass of approximately 466 kDa (*ca.* 24 subunits, monomeric mass 20.2 kDa) matches well with the value of approximately 475 kDa, which was previously determined by analytical size exclusion chromatography and interpreted as an indication for the predominance of 24-mers in αB-crystallin preparations as well as for their low polydispersity (13). In fact, however, as our detailed analysis here shows, also other oligomers (22-, 23-, 26-mers, etc.) account for the observed mean molecular mass (Fig. 5*E*). As most of the oligomers possess an almost spherical structure and differ in their dimensions only marginally (Fig. 5 and Table S1), their hydrodynamic parameters (e.g., Stokes radii and sedimentation coefficients estimated from the reconstructed EM volumes) appear also very similar (Table S1). This similarity complicates, even prevents their discrimination by dynamic light scattering or AUC, especially when some of the oligomers are present in the ensemble at low abundance.

Our findings suggest that the overall properties of αB-crystallin are dictated by the relative frequencies of different oligomer ensembles. For example, in vitro and in vivo, most of the phosphorylated forms of αB-crystallin are modified at one or two serine residues (30). In this context, the locations of the three serine residues in our models are highly interesting because they show different accessibilities for kinases in all higher-order oligomers in which the N-terminal domains are engaged in intermolecular contacts. This situation implies, also in the context of polydisperse ensemble of oligomers, unequal levels of phosphorylation at the three serine residues, which is in tune with the reported observations (30).

Higher-order αB-crystallin oligomers, in which the potential substrate-binding sites are engaged in intersubunit interactions, are likely to represent dormant storage forms. On the other hand, oligomers lacking subunits and thus exposing hydrophobic patches might contribute, together with dissociated αB-crystallin "building blocks," to the pool of "binding-competent" species. The transition of αB-crystallin from a low- to a high-affinity state presumably occurs through a remodeling of the ensemble composition by adjusting the dissociation/association rates of building blocks, determining the oligomer equilibrium according to the needs of the cell. Conditions that destabilize oligomer interfaces and lead to an enhanced rate of dissociation of subunits would raise populations of oligomers with higher binding capacity and thus increase the chaperone activity. However, an oversupply of such binding-competent oligomers could violate this delicate balance and favor aggregation or coaggregation with the client proteins. This hypothesis is coherent with in vitro studies on αB-crystallin phosphorylation-mimicking mutants which show reduced oligomer sizes, a loss of the preference for oligomers with an even number of subunits (15, 35), increased subunit exchange (36), and enhanced or even aberrant chaperone activity, depending on whether one, two, or all three serine residues are mutated (15, 35). It remains to be determined whether the emerging concept of modulating the activity of αB-crystallin by addition or subtraction of subunits from an oligomeric complex is a general phenomenon of sHsps.

In vivo, the overall activity of αB-crystallin is modulated by posttranslational modifications and/or naturally occurring mutations that presumably control its oligomeric status, and thus, its binding capacity. Myopathy-associated natural mutants of human αB-crystallin, R120G and Q151X, both hyperphosphorylated, show abnormal aggregation, abnormal intracellular distribution, and increased affinity for cytoskeletal components (37). In R120G, which is linked to cataract and desmin-related myopathy (38, 39), the loss of critical charge interactions leads to impaired stabilization of the DI interface (23, 40) concomitant with a conformational change within the interface (41), which is, according to our model, incompatible with the requirements for a proper higher-oligomer assembly. This destabilization enhances the subunit dynamics driving the dissociation of monomers or dimers (40), maladjusts the oligomer equilibrium toward an excess of assemblies with dramatically increased substrate affinity, and results in formation of insoluble coaggregates with client proteins (42).

Taken together, the excellent agreement with a plethora of experimental studies in the literature validates our structure models for αB-crystallin oligomers, which may serve as a platform for further studies to understand the modulation of its oligomer equilibrium and its consequences in the context of posttranslational modifications or disease-causing mutations in vivo.

Materials and Methods

Cloning and Protein Purification. Human αB-crystallin cysteine mutants were cloned by site-directed mutagenesis using primers bearing the respective mutation. Wild-type and mutant proteins were expressed and purified as described previously (13). The molecular masses were confirmed by MALDI-TOF mass spectrometry.

Fluorescence Quenching. Fluorescence quenching was applied to assess the accessibilities of different domains in human αB-crystallin cysteine mutants, A4C, S115C, and A172C, which were labeled with lucifer yellow iodoacetamide (LYI) (excitation wavelength 425 nm, detection wavelength 530 nm). Fluorescence was monitored in a 1.5 mL stirred cuvette with a fluorescence spectrometer (SPEX FluoroMax 1; Jobin Yvon). Quenching of LYI fluorescence was attained by stepwise addition of a 5 M sodium iodide quenching solution in PBS containing 100 mM sodium thiosulfate. The dynamic quenching constant, K_{SV}, was derived from linear fitting of Stern–Volmer plots (F_0/F vs. [Q]). Linear curve fits were obtained via the Stern–Volmer equation using ORIGIN software:

$$\frac{F_0}{F} = 1 + K_{SV}[Q]$$

with F_0 and F, fluorescence intensities in the absence and presence of quencher, respectively; K_{SV}, quenching constant (M^{-1}), and [Q], concentration of quencher (M).

Analytical Ultracentrifugation. Analytical ultracentrifugation was carried out in a Beckman XL-A ultracentrifuge with a UV detection system (Beckman Coulter). For SV measurements, 450 μL of the sample (protein concentration 40 μM) and 460 μL of the reference buffer were loaded into sector-shaped double-channel centerpieces and spun at 64,000 × *g* at 20 °C. Scans were recorded continuously at 280 nm. Data analysis was carried out by the continuous C(s) distribution method with time- and radial-invariant noise fitting using the SEDFIT software (43). The partial specific volume, buffer viscosity, and density were calculated for the applied concentrations of GdnCl.

Cross-Linking and Mass Spectrometry. Cross-linking experiments were carried out using BS3 as cross-linker. The reaction mixtures were separated into a monomer and two oligomer bands by gel electrophoresis and trypsin digested (44). Cross-linked peptides were fractionated (45), desalted (46), and analyzed on a LTQ Orbitrap Velos (Thermo Fisher Scientific) mass spectrometer (26). The data were processed using MaxQuant (47) and in-house Xi software. For details, see *SI Materials and Methods*.

Electron Microscopy. For cryo-EM, 3 μL of protein solution (0.25 mg/mL) were applied onto glow-discharged holey carbon grids, incubated for 10 s,

and plunge-frozen in liquid ethane upon blotting away the excess solution. Micrographs were recorded under low-dose conditions (approximately $10e^{-}/Å^{2}$) and at a calibrated magnification of 47,000× using a JEOL JEM 2011 transmission electron microscope operated at 120 kV. For image processing, micrographs were selected by their power spectra (33 in total) and digitized at a step size of 8.47 μm using a Flextight X5 array scanner, resulting in a pixel size of 1.8 Å at the specimen level.

Image Processing. Well-separated particle images were semimanually selected and extracted into boxes using "Boxer" from the EMAN software package (48) which was also used to determine the defoci and to correct the contrast transfer function. The defocus values of the micrographs ranged between 0.6 and 1.5 μm. All further procedures were carried out within the IMAGIC suite. For image processing, single particle images were band-pass filtered (0.5–19 nm), translationally aligned, and subjected to multivariate statistical analysis and classification. Three-dimensional reconstructions were calculated using random model reconstruction and projection matching algorithms. For details, see *SI Materials and Methods*.

Secondary Structure Prediction and Structural Modeling. Secondary structure analysis and structural modeling of αB-crystallin N- and C-terminal domains were performed using protein structure prediction servers PHYRE and I-TASSER. For details, see *SI Materials and Methods*.

Model Building. An initial model for full-length αB-crystallin was constructed by connecting the predicted structures of N- and C termini in their entire length to the structure of α-crystallin domain (23) at their respective positions using interactive modeling in CHIMERA. The pseudoatomic model of the symmetric αB-crystallin 24-mer was built by iterative docking and energy minimization cycles using the program package AMBER. For details, see *SI Materials and Methods*.

Hydrodynamic Simulations. Hydrodynamic parameters (e.g., Stokes radii), sedimentation coefficients of αB-crystallin oligomers were estimated by hydrodynamic simulations conducted within the software package HYDROMIC (49) using 3D reconstructions as input.

ACKNOWLEDGMENTS. We thank J. Plitzko, O. Mihalache, F. Förster, and Y. Georgalis for critical discussions. Z.A. Chen, L. Fischer, S. Tahir, and J.-C. Bukowski-Wills provided expert support and valuable advise for the cross-link/mass spectrometry analysis. J.B. and S.W. are funded by the Deutsche Forschungsgemeinschaft (SFB594). J.P. acknowledges a Ph.D. scholarship from the Studienstiftung des deutschen Volkes.

1. Bloemendal H, et al. (2004) Ageing and vision: Structure, stability and function of lens crystallins. *Prog Biophys Mol Biol* 86:407–485.
2. Delaye M, Tardieu A (1983) Short-range order of crystallin proteins accounts for eye lens transparency. *Nature* 302:415–417.
3. Horwitz J (1992) α-crystallin can function as a molecular chaperone. *Proc Natl Acad Sci USA* 89:10449–10453.
4. Bloemendal H (1977) The vertebrate eye lens. A useful system for the study of fundamental biological processes on a molecular level. *Science* 197:127–138.
5. de Jong WW, Caspers GJ, Leunissen JAM (1998) Genealogy of the α-crystallin-small heat-shock protein superfamily. *Int J Biol Macromol* 22:151–162.
6. Kriehuber T, et al. (2010) Independent evolution of the core domain and its flanking sequences in small heat shock proteins. *FASEB J* 24:3633–3642.
7. Iwaki T, Kuma-Iwaki A, Goldman JE (1990) Cellular distribution of αB-crystallin in non-lenticular tissues. *J Histochem Cytochem* 38:31–39.
8. Klemenz R, Fröhli E, Steiger RH, Schäfer R, Aoyama A (1991) αB-crystallin is a small heat shock protein. *Proc Natl Acad Sci USA* 88:3652–3656.
9. Iwaki T, Kuma-Iwaki A, Liem RK, Goldman JE (1989) αB-crystallin is expressed in non-lenticular tissues and accumulates in Alexander's disease brain. *Cell* 57:71–78.
10. van Noort JM (1995) The small heat-shock protein αB-crystallin as candidate auto-antigen in multiple sclerosis. *Nature* 375:798–801.
11. Ousman SS, et al. (2007) Protective and therapeutic role for αB-crystallin in autoimmune demyelination. *Nature* 448:474–479.
12. Launay N, Tarze A, Vicart P, Lilienbaum A (2010) Serine 59 phosphorylation of αB-crystallin down-regulates its anti-apoptotic function by binding and sequestering Bcl-2 in breast cancer cells. *J Biol Chem* 285:37324–37332.
13. Peschek J, et al. (2009) The eye lens chaperone α-crystallin forms defined globular assemblies. *Proc Natl Acad Sci USA* 106:13272–13277.
14. Aquilina JA, Benesch JLP, Bateman OA, Slingsby C, Robinson CV (2003) Polydispersity of a mammalian chaperone: Mass spectrometry reveals the population of oligomers in αB-crystallin. *Proc Natl Acad Sci USA* 100:10611–10616.
15. Aquilina JA, et al. (2004) Phosphorylation of αB-crystallin alters chaperone function through loss of dimeric substructure. *J Biol Chem* 279:28675–28680.
16. Benesch JLP, Ayoub M, Robinson CV, Aquilina JA (2008) Small heat shock protein activity is regulated by variable oligomeric structure. *J Biol Chem* 283:28513–28517.
17. Sun T-X, Liang JJ-N (1998) Intermolecular exchange and stabilization of recombinant human αA- and αB-crystallin. *J Biol Chem* 273:286–290.
18. Haley DA, Horwitz J, Stewart PL (1998) The small heat-shock protein, αB-crystallin, has a variable quaternary structure. *J Mol Biol* 277:27–35.
19. Kim KK, Kim R, Kim SH (1998) Crystal structure of a small heat-shock protein. *Nature* 394:595–599.
20. Haslbeck M, Kastenmüller A, Buchner J, Weinkauf S, Braun N (2008) Structural dynamics of archaeal small heat shock proteins. *J Mol Biol* 378:362–374.
21. Bagneris C, et al. (2009) Crystal structures of α-crystallin domain dimers of αB-crystallin and Hsp20. *J Mol Biol* 392:1242–1252.
22. Laganowsky A, et al. (2010) Crystal structures of truncated alphaA and alphaB crystallins reveal structural mechanisms of polydispersity important for eye lens function. *Protein Sci* 19:1031–1043.
23. Jehle S, et al. (2010) Solid-state NMR and SAXS studies provide a structural basis for the activation of αB-crystallin oligomers. *Nat Struct Mol Biol* 17:1037–1042.
24. Jehle S, et al. (2011) N-terminal domain of αB-crystallin provides a conformational switch for multimerization and structural heterogeneity. *Proc Natl Acad Sci USA* 108:6409–6414.
25. Rappsilber J (2011) The beginning of a beautiful friendship: Cross-linking/mass spectrometry and modelling of proteins and multi-protein complexes. *J Struct Biol* 173:530–540.
26. Chen ZA, et al. (2010) Architecture of the RNA polymerase II-TFIIF complex revealed by cross-linking and mass spectrometry. *EMBO J* 29:717–726.
27. Carver JA, Aquilina JA, Truscott RJ, Ralston GB (1992) Identification by ^{1}H-NMR spectroscopy of flexible C-terminal extensions in bovine lens α-crystallin. *FEBS Lett* 311:143–149.
28. Pasta SY, Raman B, Ramakrishna T, Rao C (2004) The IXI/V motif in the C-terminal extension of α-crystallins: Alternative interactions and oligomeric assemblies. *Mol Vis* 10:655–662.
29. Thampi P, Abraham EC (2003) Influence of the C-terminal residues on oligomerization of αA-crystallin. *Biochemistry* 42:11857–11863.
30. Ito H, Okamoto K, Nakayama H, Isobe T, Kato K (1997) Phosphorylation of αB-crystallin in response to various types of stress. *J Biol Chem* 272:29934–29941.
31. Sharma KK, Kumar RS, Kumar GS, Quinn PT (2000) Synthesis and characterization of a peptide identified as a functional element in αA-crystallin. *J Biol Chem* 275:3767–3771.
32. Ghosh JG, Shenoy AK, Clark JI (2006) N- and C-terminal motifs in human αB crystallin play an important role in the recognition, selection, and solubilization of substrates. *Biochemistry* 45:13847–13854.
33. Aquilina JA, Watt SJ (2007) The N-terminal domain of αB-crystallin is protected from proteolysis by bound substrate. *Biochem Biophys Res Commun* 353:1115–1120.
34. Plater ML, Goode D, Crabbe MJ (1996) Effects of site-directed mutations on the chaperone-like activity of αB-crystallin. *J Biol Chem* 271:28558–28566.
35. Ecroyd H, et al. (2007) Mimicking phosphorylation of αB-crystallin affects its chaperone activity. *Biochem J* 401:129–141.
36. Ahmad MdF, Raman B, Ramakrishna T, Rao ChM (2008) Effect of phosphorylation on αB-crystallin: Differences in stability, subunit exchange and chaperone activity of homo and mixed oligomers of αB-crystallin and its phosphorylation-mimicking mutant. *J Mol Biol* 375:1040–1051.
37. Simon S, et al. (2007) Myopathy-associated αB-crystallin mutants. Abnormal phosphorylation, intracellular localition, and interactions with other small heat shock proteins. *J Biol Chem* 282:34276–34287.
38. Vicart P, et al. (1998) A missense mutation in the αB-crystallin chaperone gene causes a desmin-related myopathy. *Nat Genet* 20:92–95.
39. Rajasekaran NS, et al. (2007) Human alpha B-crystallin mutation causes oxido-reductive stress and protein aggregation cardiomyopathy in mice. *Cell* 130:427–439.
40. Michiel M, et al. (2009) Abnormal assemblies and subunit exchange of αB-crystallin R120 mutants could be associated with destabilization of the dimeric substructure. *Biochemistry* 48:442–453.
41. Clark AR, Naylor CE, Bagneris C, Keep NH, Slingsby C (2011) Crystal structure of R120G disease mutant of human αB-crystallin domain dimer shows closure of a groove. *J Mol Biol* 408:118–134.
42. Bova MP, et al. (1999) Mutation R120G in αB-crystallin which is linked to a desmin-related myopathy, results in an irregular structure and defective chaperone-like function. *Proc Natl Acad Sci USA* 96:6137–6142.
43. Schuck P (2000) Size distribution analysis of macromolecules by sedimentation velocity ultracentrifugation and Lamm equation modeling. *Biophys J* 78:1606–1619.
44. Maiolica A, et al. (2007) Structural analysis of multiprotein complexes by cross-linking, mass spectrometry, and database searching. *Mol Cell Proteomics* 6:2200–2211.
45. Rappsilber J, Mann M, Ishihama Y (2007) Protocol for micro-purification, enrichment, pre-fractionation and storage of peptides for proteomics using StageTips. *Nat Protoc* 2:1896–906.
46. Rappsilber J, Ishihama Y, Mann M (2003) Stop and go extraction tips for matrix-assisted laser desorption/ionization, nanoelectrospray, and LC/MS sample pretreatment in proteomics. *Anal Chem* 75:663–670.
47. Cox J, Mann M (2008) MaxQuant enables high peptide identification rates, individualized p.p.b.-range mass accuracies and proteome-wide protein quantification. *Nat Biotechnol* 26:1367–1372.
48. Ludtke SJ, Baldwin PR, Chiu W (1999) EMAN: Semiautomated software for high-resolution single particle reconstructions. *J Struct Biol* 128:82–97.
49. de la Torre JG, Valpuesta JM, Carrascosa JL (2001) HYDROMIC: Prediction of hydrodynamic properties of rigid macromolecular structures obtained from electron-microscopy images. *Eur Biophys J* 30:457–462.